The Diffraction Response Interpolation Method

Søren K. Jespersen, Peder C. Pedersen, *Senior Member, IEEE*, and Jens E. Wilhjelm, *Member, IEEE*

Abstract—**Computer modeling of the output voltage in a pulse-echo system is computationally very demanding, particularly when considering reflector surfaces of arbitrary geometry. A new, efficient computational tool, the diffraction response interpolation method (DRIM), for modeling of reflectors in a fluid medium, is presented. The DRIM is based on the velocity potential impulse response method, adapted to pulse-echo applications by the use of acoustical reciprocity. Specifically, the DRIM operates by dividing the reflector surface into planar elements, finding the diffraction response at the corners of the elements, calculating the response integrated over the surface element by time-domain convolutions with analytically determined filters, and summing the responses from the individual surface elements. As the method is based on linearity, effects such as shadowing, higher-order diffraction, nonlinear propagation, cannot be directly incorporated in the modeling. The DRIM has been compared to other modeling tools when possible. Excellent agreement between the results obtained with the DRIM and the alternative techniques have been found, and the DRIM offers reductions in computation time in the range from 30 to 400 times. Experimental results obtained using a planar circular transducer together with cylindrical reflectors were compared to DRIM results and fairly good agreement was observed.**

I. Introduction

MEDICAL applications of ultrasound have been primarily for qualitative imaging purposes, and progress in development of more quantitative techniques, such as tissue characterization, classification of surface topology, have been slow. One reason for the slow progress is the large number of factors that determine the output voltage in a pulse-echo system. These include: parameters of the transmit and receive transducers such as geometry, location, electro-acoustic and acousto-electric transfer functions, excitation, etc.; coupling medium parameters such as speed of sound, attenuation, absorption, refraction, scattering (including possible spatial variations of these); and parameters of the reflecting structure such as size, surface geometry, acoustic impedance, location, and orientation. Efficient tools for modeling pulse-echo systems, therefore, are important for further development of advanced diagnostic techniques, as well as for nondestructive testing (NDT). Potential applications of such modeling tools include:

- Understanding and quantification of the influences of reflector geometry and orientation, possibly leading to understanding of, and compensation for, artifacts in imaging and quantitative analysis.
- Development of systems optimized for extraction of quantitative information about the object under investigation (e.g., surface irregularity) by proper selection of transmit and receive transducers, focusing and apodization strategies, etc.
- Determination of optimal signal processing of the output voltages to extract classification features for the object under investigation.
- Application as part of an iterative inverse tool for determination of reflector characteristics from one or more output voltage waveforms. An example could be iterative determination of tilt angle or surface roughness.

As the computational power available is steadily increasing, application of more advanced pulse-echo modeling techniques have become reality, opening the possibility for modeling of situations closer to real-world situations. Modeling techniques for pulse-echo systems can be grouped into four main categories: analytical approaches, angular spectrum methods, finite-element methods, and impulse response-based approaches.

Analytical approaches currently are limited to simple situations like infinite planar specular reflectors at normal incidence [1], [2] and, therefore, are not of much interest in general modeling.

The angular spectrum methods are based on a decomposition of the acoustic field into plane waves, the so-called angular spectrum decomposition (ASD). The use of ASD methods for modeling of pulse-echo systems has until now been restricted to applications involving infinite and finite planar reflectors [3], [4]. Recently, ASD has been applied in modeling of reflections from planar rough surfaces [5]. Unfortunately, the ASD-methods are very computationally intensive when applied for pulse-echo modeling, thereby limiting the applicability for general reflector geometries.

Finite-element methods mainly have been used as a CAD-tool in design of piezo-electric elements in ultrasound transducers [6]. Recently, finite-element methods also have been applied to modeling of an entire pulse-echo system, as demonstrated by Lerch *et al.* [7], [8]. The main advantage of the finite-element analysis approach is that very complex, and thus more realistic, physical situations can be modeled, including nonideal vibrational behavior of the

Manuscript received August 27, 1996; accepted April 8, 1998. CADUS (Center for Arteriosclerosis Detection with UltraSound) is supported by the Danish Technical Research Council and the Danish Medical Research Council.

S. K. Jespersen is with B-K Medical, Sandtoften 9, DK-2820 Gentofte, Denmark (e-mail: skj@bkmed.dk).

P. C. Pedersen is with the Department of Electrical and Computer Engineering, Worcester Polytechnic Institute, Worcester, MA 01609.

J. E. Wilhjelm is with CADUS, Department of Information Technology, Technical University of Denmark, DK-2800 Lyngby, Denmark.

transducer elements, inhomogeneous coupling media and deformation of the reflecting obstacles. A drawback of the finite-element method is the computation time; nevertheless, it is likely that finite-element modeling will gain momentum as computational power continues to increase.

Methods based on the velocity potential impulse response [9] are currently widely used for calculation of pressure fields and pulse-echo responses from point-like scatterers. Generally, a homogeneous, nonattenuating fluid medium is assumed, but simple frequency dependent attenuation can be incorporated in the modeling [10]. An analysis of diffraction effects, based on impulse response methods and their influence on the use of pulse-echo ultrasound measurements in medical diagnosis, is described in Fink and Cardoso [11]. The method also has been applied to evaluate focusing strategies [12], simulation of image formation [12], simulation of speckle in ultrasound images [13], and for simulation of Doppler systems [12], [14]. The impulse response methods can be broadened further to cover calculation of output voltages due to extended reflector surfaces [15], [16]. The method also has been considered by Lhémery [17] and Lhémery and Raillon [18], in which the theory and computer implementation have been described in more detail. A similar approximative method also has been used by Oh *et al.* [19] for calculation of the output voltage due to an undulating surface, for the purpose of characterizing periodic surfaces.

II. Background

The theory of the velocity potential impulse response methods is well-known [9] and will not be described here. The impulse response based methods may be applied to pulse-echo modeling of the output voltage due to a rigid point scatterer, as described by Weight and Hayman [20]. Consider a transducer insonifying a rigid point scatterer with a surface area dA, located at a field point $\vec{r}$ in a homogeneous medium with speed of sound c and density ρ_0. The output voltage, $dv_p(\vec{r},t)$, due to the point scatterer will be proportional to the pressure integrated over the transducer surface [16]:

$$dv_p(\vec{r},t) = -\frac{dA\,\rho_0}{2c} g_r(t) \otimes u_{tx}(t) \otimes \frac{\partial^2}{\partial t^2}\left(h_t(\vec{r},t) \otimes h_r(\vec{r},t)\right) \quad (1)$$

where $u_{tx}(t)$ is the surface velocity of the transducer, $g_r(t)$ is the acousto-electrical impulse response of the receiving transducer (i.e., the electrical response due to an impulsive force on the transducer surface), $h_t(\vec{r},t)$ and $h_r(\vec{r},t)$ are the velocity potential impulse responses for the transmit aperture and the receive aperture, respectively. To simplify the notation, the pulse-echo diffraction impulse response (or diffraction response for short), $D(\vec{r},t)$, is defined as:

$$D(\vec{r},t) = \frac{\partial^2}{\partial t^2}\left(h_t(\vec{r},t) \otimes h_r(\vec{r},t)\right). \quad (2)$$

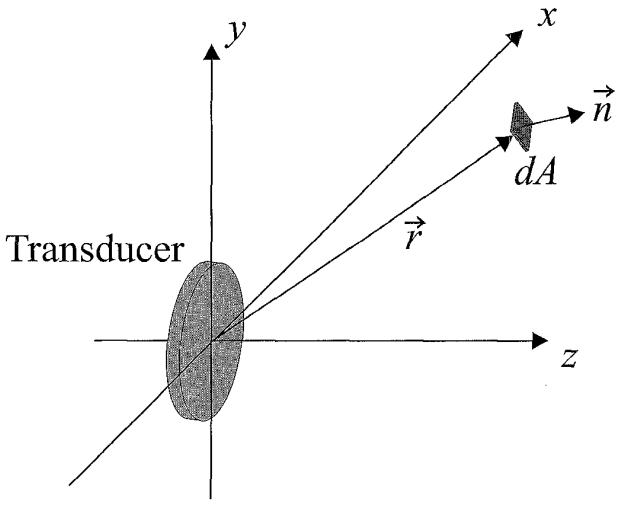

Fig. 1. Pulse-echo system with transducer insonifying a planar reflector with area dA and unit normal vector $\vec{n}$. The center of the reflector is located at the field point identified by $\vec{r}$.

The output voltage due to an extended reflector surface, A, can be found by application of linearity if a given set of assumptions are fulfilled (to be described later). The pressure reflection coefficient is R_0, for a plane pressure wave at normal incidence. In this case, the output voltage can be found by summing (integrating) the responses from all points on the reflector surface. The response from an infinitesimally small area, dA, of the surface can be found if the normal velocity, $u_n(\vec{r},t)$, of the reflecting surface at the area dA can be determined. Consider the situation depicted in Fig. 1 in which a small surface element of the extended reflector is illustrated. The small surface element has an area dA, a unit normal vector $\vec{n}$, and is located with its center at the field point given by $\vec{r}$. The incident pressure is denoted $p_i(\vec{r},t)$. If $\vec{u}(\vec{r},t)$ is the particle velocity vector at $\vec{r}$, then the normal velocity of the small reflector, $u_n(\vec{r},t)$, can be found, assuming the field to be locally plane, as:

$$u_n(\vec{r},t) = \frac{p_i(\vec{r},t)}{\rho_0 c}\frac{\vec{u}(\vec{r},t)\cdot\vec{n}}{|\vec{u}(\vec{r},t)|} = \frac{p_i(\vec{r},t)}{\rho_0 c}\frac{\nabla h_t(\vec{r},t)\cdot\vec{n}}{|\nabla h_t(\vec{r},t)|} = \frac{p_i(\vec{r},t)}{\rho_0 c}\cos[\theta(\vec{r},t)] \quad (3)$$

where $\theta(\vec{r},t)$ is is the time-varying angle between $\vec{n}$ and $\vec{u}(\vec{r},t)$. In general (3) is too computationally demanding to evaluate, and some approximation of $\cos(\theta(\vec{r},t))$ must be used. Two approximations may be considered, one being valid when the transducer is a point source (spherical wave):

$$\cos[\theta(\vec{r},t)] \cong \cos(\theta(\vec{r})) = \frac{\vec{r}\cdot\vec{n}}{|\vec{r}|} \quad (4)$$

and another being valid when the insonifying field can be considered a plane wave, propagating in the z-direction:

$$\cos[\theta(\vec{r},t)] \cong \cos(\theta(\vec{r})) = \hat{z}\cdot\vec{n} \quad (5)$$

where $\hat{z}$ is a unit vector in the z-direction. For field points on the acoustic axis, the two approximations yield the same value, and near the axis the difference will be small. The $\cos(\theta)$-factor is only an amplitude correction, which in general is much less important than a phase correction. From now on (5) is used, consequently $\theta(\vec{r},t) = \theta(\vec{r})$.

By application of (1) (with a scale factor of two because the reflector is now part of an extended, locally smooth reflector [17]) and (3), the output voltage due to the small element of the reflector surface, $dv(\vec{r},t)$ can be shown to be:

$$dv(\vec{r},t) = \frac{R_0\rho_0}{c}\cos[\theta(\vec{r})]g_r(t) \otimes u_{tx}(t) \otimes D(\vec{r},t)\,dA. \tag{6}$$

By applying the principle of linearity, the output voltage due to the extended reflector surface, $v_{\text{surf}}(t)$, can be found by integrating the response over the reflector surface:

$$v_{\text{surf}}(t) = Kg_r(t) \otimes u_{tx}(t) \otimes \int_A \cos[\theta(\vec{r})]D(\vec{r},t)dA \tag{7}$$

where $K = R_0\rho_0/c$.

The expression in (7) is derived assuming linearity, consequently all effects due to higher-order diffraction phenomena, such as shadowing effects and angle dependent reflection coefficients cannot be included in the modeling. These assumptions put limitations on the geometry of the surfaces that can be modeled with good precision, e.g., very irregular surfaces cannot be modeled, as second-order diffraction and shadowing must be considered to obtain correct results. Also, very concave surfaces where significant higher-order diffraction could occur must be treated with care.

Equation (7) is appealing in the sense that it is simple to determine the output voltage assuming that $h(\vec{r},t)$ or $D(\vec{r},t)$ is available. Unfortunately, if a discrete implementation of (7) is made (i.e., the responses are calculated at discrete points on the surface and summed) a very large number of surface points must be used, whenever the reflector surface has even a small tilt relative to normal incidence. As a pulse-echo ultrasound system is coherent (or alternatively phase-sensitive), the relative phase of the received signal from each surface element must be preserved, otherwise very significant errors due to erroneous phase cancellation might occur. This is illustrated by investigating the spatial variation of a pulsed field. This variation is in general quite complex, but in the axial direction of the beam the variation is known, at least if the field is considered locally plane. Assume that the pulsed field is band-limited with a maximum frequency of $f_{\max} = 15$ MHz and propagates in a medium with $c = 1500$ m/s. The minimum wavelength is then $\lambda_{\min} = c/f_{\max} = 100$ μm. If the reflector tilt angle is 20° and the maximum phase error over the surface elements in the discrete evaluation of (7) that will be accepted is $\pi/10$ radians, corresponding to 0.05 wavelength (which in turn translates into $\simeq 1.25\%$ amplitude error when adding continuous wave signals), the maximum distance between surface points becomes $\Delta d = 0.05\lambda_{\min}/\sin(20°) = 14.6$ μm. If this distance is used for evaluating the response from a 15×15 mm reflector, the number of surface points becomes $1.05 \cdot 10^6$ which in turn leads to unacceptable computation times. The aim of the DRIM is a computationally efficient calculation of (7) while maintaining a satisfactory precision.

III. Theory

The approach of the DRIM is to determine the output voltage due to an extended reflector by dividing the reflector into planar reflector elements (tiles) of moderate dimensions, calculate the contribution from each tile, and sum the responses. This overall principle is identical to the "Huygen" approach described previously [i.e., discrete evaluation of (7)], but the DRIM uses an alternative approach allowing for much larger tiles. The DRIM calculates the integral of the diffraction response over the tile by approximating the true diffraction response at any point on the tile to a diffraction response interpolated in time (and optionally amplitude) between the responses from the corners of the tile. It will be shown that the integral of the interpolated diffraction response over the tile can be expressed in a computationally very efficient way by time-domain filterings with simple filters determined by the delay (and optionally amplitude) differences of the responses from the corners of the tile.

In order to further simplify the notation, the terms $u_{tx}(t)$ and $g_r(t)$ will not be included specifically in the expressions for the output voltages in this section. The terms are reintroduced in the final equation (46) for the output voltage. This does not limit the applicability of the approach, as realistic functions for $u_{tx}(t)$ and $g_r(t)$ can be convolved on to the calculated responses at any point in the process, due to the assumed linearity.

A. Output Voltage from a Line Reflector

In this subsection the basic interpolation principle will be derived for the case of a simple line reflector, C_R, of width dw and arc length L. This is done to obtain a solution for the simple one-dimensional problem; next the solutions for two-dimensional rectangular tiles will be developed. The reflector is assumed to be much narrower than the smallest wavelength of the incident pressure waveform, and L is some specified finite length. The ends of the line source are specified by the two position vectors $\vec{r}_1$ and $\vec{r}_{N+1}$, as illustrated in Fig. 2. The output voltage due to the line reflector, $v_{\text{line}}(t)$, can be found by application of (7) to be:

$$v_{\text{line}}(t) = Kdw \int_{C_R} \cos[\theta(\vec{r})]D(\vec{r},t)dl. \tag{8}$$

This integral may be evaluated numerically, based on the Huygen approach, by dividing the line reflector into a very large number of segments, N. The segmentation of L is defined by points on the line reflector such that the position

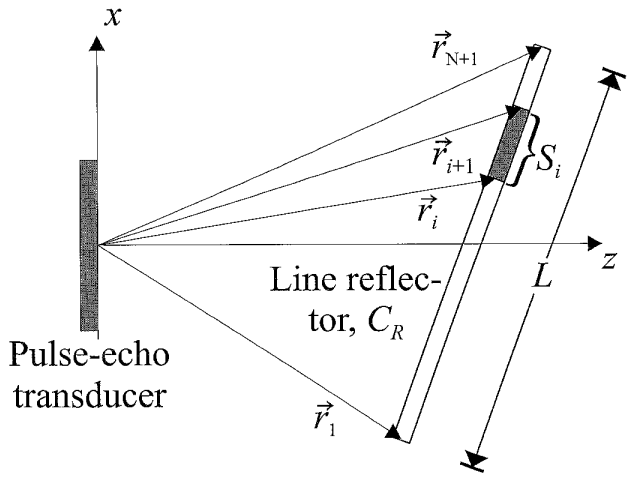

Fig. 2. Line reflector in front of pulse-echo transducer. The end points of the line reflector are identified by the position vectors $\vec{r}_1$ and $\vec{r}_{N+1}$, respectively. A specific line segment of length S_i, limited by the position vectors $\vec{r}_i$ and $\vec{r}_{i+1}$, is shown.

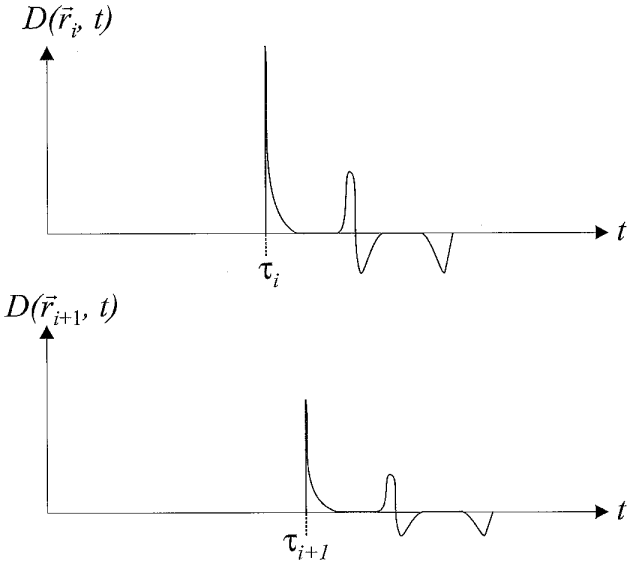

Fig. 3. Hypothetical diffraction responses for two points situated not too far from each other.

vectors $\vec{r}_i$ and $\vec{r}_{i+1}$ identify the beginning and the end of segment i, respectively. Assuming that N is chosen large enough, $v_{\text{line}}(t)$ is approximated well by:

$$v_{\text{line}}(t) = Kdw \sum_{i=1}^{N} \cos[\theta(\vec{r}_i)] S_i D(\vec{r}_i, t) \tag{9}$$

where S_i is the length of the ith segment.

Now a computationally more efficient approach will be presented that allows the line reflector to be divided into a much lower number of segments, N, with larger lengths. Assume that the contribution due to the line segment in Fig. 2 is to be found. When S_i is chosen to be of moderate length, $D(\vec{r}_i, t)$ and $D(\vec{r}_{i+1}, t)$ will, in general, not differ much in waveform (shape), but rather be shifted in time. The degree of change in the waveform is dependent on the segment length, transducer type and focusing scheme, reflector orientation, field point location, etc. Two hypothetical diffraction responses are depicted in Fig. 3, in which the shape is maintained, but the signals are scaled in amplitude and shifted in time, such that the response at point $\vec{r}_i$ starts at time $t = \tau_i$ and the response at point $\vec{r}_{i+1}$ starts at time $t = \tau_{i+1}$.

1. Linearization of Diffraction Responses: Now, let the response $D(\vec{r}, t)$ be expressed as:

$$D(\vec{r}, t) = D_0(\vec{r}, t - \tau) = \delta(t - \tau) \otimes D_0(\vec{r}, t) \tag{10}$$

where $D_0(\vec{r}, t)$ is the response at $\vec{r}$, but with the delay, τ, from $t = 0$ to the beginning of the response removed. The linearization of $D(\vec{r}, t)$, between the field points $\vec{r}_i$ and $\vec{r}_{i+1}$ is made by linearizing the change in amplitude of $D_0(\vec{r}, t)$ over the range between $\vec{r}_i$ and $\vec{r}_{i+1}$ and assigning a delay, linearized between $t = \tau_i$ and $t = \tau_{i+1}$, to the linearized version of $D_0(\vec{r}, t)$. The linearized waveform for the ith segment, $D_{0,i}(l, t)$, over the range $\vec{r} \in [\vec{r}_i; \vec{r}_{i+1}]$ can be expressed as:

$$D_{0,i}(l, t) = D_0(\vec{r}_i, t) + \frac{D_0(\vec{r}_{i+1}, t) - D_0(\vec{r}_i, t)}{S_i} l, \quad l \in [0; S_i] \tag{11}$$

where l is a spatial length variable, such that $l = 0$ for $\vec{r} = \vec{r}_i$ and $l = S_i$ for $\vec{r} = \vec{r}_{i+1}$. Note that $D_{0,i}(l, t)$ in (11) is no longer a function of $\vec{r}$, but rather a function of l. It is seen that the linearization described in (11) is actually an amplitude linearization, because it will correctly describe a uniform scaling of the waveform, but not a change in shape, such as a compression or expansion in time. The associated linearized delay for the ith segment, $\tau_i(l)$, is likewise a function of l only and can be expressed as:

$$\tau_i(l) = \tau_i + \frac{\tau_{i+1} - \tau_i}{S_i} l, \quad l \in [0; S_i] \tag{12}$$

2. Integration of Linearized Diffraction Response: Applying (10), (11), and (12) in (8) and omitting the obliquity factor $\cos[\theta(\vec{r})]$ for later reintroduction, the expression for the output voltage due to the ith line segment, $v_i(t)$, becomes:

$$\begin{aligned} v_i(t) &= Kdw \int_0^{S_i} D_{0,i}(l, t) \otimes \delta(t - \tau_i(l)) dl \\ &= Kdw \int_0^{S_i} \delta(t - \tau_i(l)) \otimes \\ &\quad \left[D_0(\vec{r}_i, t) + \frac{D_0(\vec{r}_{i+1}, t) - D_0(\vec{r}_i, t)}{S_i} l \right] dl. \end{aligned} \tag{13}$$

Because the functions $D_0(\vec{r}_i, t)$ and $D_0(\vec{r}_{i+1}, t)$ do not depend on l, (13) can be written as:

$$v_i(t) = K dw D_0(\vec{r}_i, t) \otimes \int_0^{S_i} \delta(t - \tau_i(l))\, dl + K dw\, \Delta D_0(\vec{r}_i, t) \otimes \frac{1}{S_i} \int_0^{S_i} l\, \delta(t - \tau_i(l))\, dl \quad (14)$$

where $\Delta D_0(\vec{r}_i, t)$ is the difference signal:

$$\Delta D_0(\vec{r}_i, t) = D_0(\vec{r}_{i+1}, t) - D_0(\vec{r}_i, t). \quad (15)$$

The difference signal will in general carry much less energy than the original response $D_0(\vec{r}_i, t)$ because $\Delta D_0(\vec{r}_i, t)$ represents only the change in waveform of the diffraction response from one end of the line segment to the other.

Equation (14) contains two integrals; the first integral will be denoted $A_i(t)$ and the second integral will be denoted $B_i(t)$; [$A_i(t)$ and $B_i(t)$ are defined specifically in (49) and (50)]. In Appendix A, $A_i(t)$ is shown to be a rectangular time function, as specified in (61), and $B_i(t)$ is shown to be a triangular time function, as given by (63).

Now the output voltage due to the ith line segment, $v_i(t)$, can be found by application of (14), (61), and (63):

$$v_i(t) = K dw \cos[\theta(\vec{r}_i)][D_0(\vec{r}_i, t) \otimes A_i(t) + \Delta D_0(\vec{r}_i, t) \otimes B_i(t)] \quad (16)$$

where the obliquity factor, $\cos[\theta(\vec{r}_i)]$, is reintroduced. The output voltage due to the line reflector can then be expressed as:

$$v_{\text{line}}(t) = \sum_{i=1}^{N} v_i(t)$$

B. Output Voltage from a Finite Surface Tessellated into Rectangular Tiles

The full utility of the DRIM is only achieved when the output voltage can be determined for an extended finite reflector of arbitrary geometry. In this section the DRIM will be extended to cover efficient calculation of the responses due to rectangular tiles. The modeling situation is depicted in Fig. 4.

The tiles tessellating the surface must be chosen so that they approximate the surface well; consequently, smaller tiles must be used when the surface is strongly curved. Also, if the rate of change of $D_0(\vec{r}, t)$ along the reflector is large, small tiles must be chosen, similar to what was described for the line segments in Section III,A.

1. Definition of Pulse-Echo Diffraction Parameters: The calculation of the response due to a single rectangular tile will now be considered, as illustrated in Fig. 5. The tile is placed in a local uv-coordinate system and has a side length U in the u-direction and a side length V in the v-direction. The corners of the tile are identified by the position vectors $\vec{r}_{0,0}$, $\vec{r}_{1,0}$, $\vec{r}_{0,1}$, and $\vec{r}_{1,1}$, where $\vec{r}_{0,0}$ corresponds to $(u, v) = (0, 0)$, $\vec{r}_{1,0}$ corresponds to $(u, v) = (U, 0)$, $\vec{r}_{0,1}$ corresponds to $(u, v) = (0, V)$, and $\vec{r}_{1,1}$ corresponds to $(u, v) = (U, V)$. The delays to the start of the diffraction responses at the four corners are denoted $\tau_{0,0}$, $\tau_{1,0}$, $\tau_{0,1}$, and $\tau_{1,1}$, respectively. The linearized diffraction response on the tile surface with the delay removed is $D_0(u, v, t)$ and the linearized delay on the tile surface is $\tau(u, v)$.

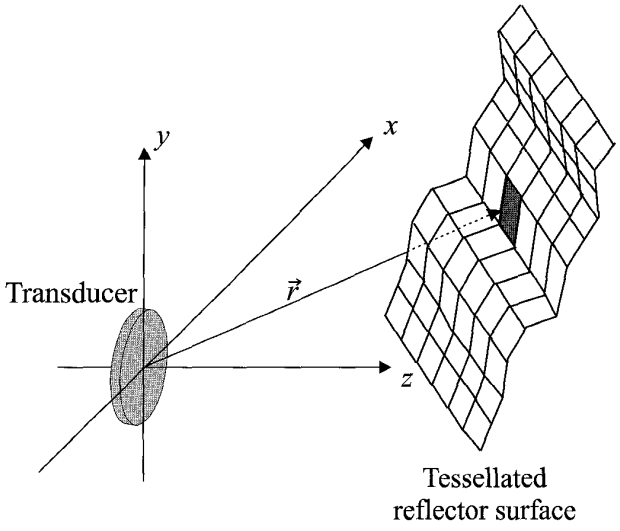

Fig. 4. Illustration of pulse-echo system with transducer and reflector surface, tessellated into planar rectangular tiles.

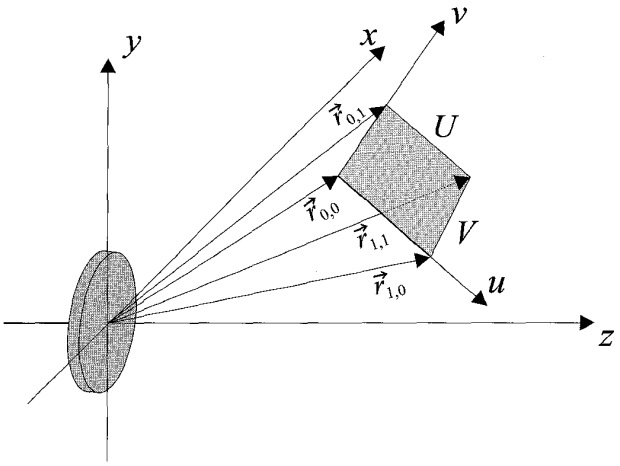

Fig. 5. Illustration of pulse-echo system with transducer and a single rectangular tile, placed in a local uv-coordinate system. The tile has side lengths U and V in the u- and v-directions, respectively.

2. Delay Linearization: The linearization of the delay follows the approach used for the line reflector, with appropriate modifications. The 2D linearization task for the rectangular tile is a little more complicated than the 1D linearization for the line reflector segment, as four delay values must be considered here. Because the resulting delay function, $\tau(u, v)$, must be linear, only three delay values are required for specifying the delay plane. Thus, the

four delay values over-specify the delay plane, and some approach to finding a "best matching" delay plane must be introduced. An approach could be to employ a bilinear delay function, but this would introduce nonlinear terms that in turn may prevent the development of analytical solutions.

The approach to defining a suitable delay plane that will be taken here is to find a least squares linearization plane, i.e., defining a set of four "adjusted" delay values, $\tau^c_{0,0}$, $\tau^c_{1,0}$, $\tau^c_{0,1}$, and $\tau^c_{1,1}$ for the four corners chosen such that they fall into a plane and such that the mean square error, E_{del}, is minimized:

$$E_{\text{del}} = \frac{1}{4}\sum \epsilon^2_{j,k}, \quad j = 0,1; k = 0,1 \tag{17}$$

where $\epsilon_{j,k} = \tau^c_{j,k} - \tau_{j,k}$ is the delay error at the corner labeled by j,k. The delay linearization plane can then be described as:

$$\begin{aligned}\tau(u,v) &= \tau^c_{0,0} + \frac{\tau^c_{1,0} - \tau^c_{0,0}}{U}\,u + \frac{\tau^c_{0,1} - \tau^c_{0,0}}{V}\,v \\ &= \tau^c_{0,0} + \Gamma_u\,u + \Gamma_v\,v\end{aligned} \tag{18}$$

where Γ_u and Γ_v are the delay slopes in the u- and v-direction, respectively:

$$\Gamma_u = \frac{\tau^c_{1,0} - \tau^c_{0,0}}{U} \tag{19}$$

$$\Gamma_v = \frac{\tau^c_{0,1} - \tau^c_{0,0}}{V}. \tag{20}$$

The least squares solution can be determined as described in Appendix B, and the resulting expressions are found by tedious, but straightforward, calculations to be:

$$\tau^c_{0,0} = \frac{1}{4}\left[3\tau_{0,0} + \tau_{1,0} + \tau_{0,1} - \tau_{1,1}\right] \tag{21}$$

$$\Gamma_u = \frac{1}{2U}\left[-\tau_{0,0} + \tau_{1,0} - \tau_{0,1} + \tau_{1,1}\right] \tag{22}$$

$$\Gamma_v = \frac{1}{2V}\left[-\tau_{0,0} - \tau_{1,0} + \tau_{0,1} + \tau_{1,1}\right] \tag{23}$$

3. Amplitude Linearization: The linearization procedure for the amplitude follows the least squares procedure for the delay. This approach requires that the amplitude scaling information be expressed as a single value for each diffraction response. This number could, for example, be the square root of the energy of the response, $M_{j,k}$:

$$M_{j,k} = \sqrt{\int_{-\infty}^{\infty} \left[D(\vec{r}_{j,k}, t)\right]^2 dt}, \quad j = 0,1;\ k = 0,1. \tag{24}$$

A least squares amplitude linearization plane then can be defined by minimizing the mean square error, E_{ampl}:

$$E_{\text{ampl}} = \frac{1}{4}\sum \left(M^c_{j,k} - M_{j,k}\right)^2, \quad j = 0,1;\ k = 0,1 \tag{25}$$

leading to a set of linearized amplitude factors, $M^c_{j,k}$, that will all fall in the linearization plane. The minimization solution can be found, by following the approach from the delay linearization, to be:

$$M^c_{0,0} = \frac{1}{4}\left[3M_{0,0} + M_{1,0} + M_{0,1} - M_{1,1}\right] \tag{26}$$

$$M^c_{1,0} = \frac{1}{4}\left[M_{0,0} + 3M_{1,0} - M_{0,1} + M_{1,1}\right] \tag{27}$$

$$M^c_{0,1} = \frac{1}{4}\left[M_{0,0} - M_{1,0} + 3M_{0,1} + M_{1,1}\right] \tag{28}$$

$$M^c_{1,1} = \frac{1}{4}\left[-M_{0,0} + M_{1,0} + M_{0,1} + 3M_{1,1}\right]. \tag{29}$$

An amplitude "adjusted" set of diffraction responses with the delay removed can now be defined as:

$$D^c_0(\vec{r}_{j,k}, t) = \frac{M^c_{j,k}}{M_{j,k}} D_0(\vec{r}_{j,k}, t), \quad j = 0,1;\ k = 0,1. \tag{30}$$

The linearized diffraction response (with the delay removed) over the tile can now be expressed as:

$$\begin{aligned}D_0(u,v,t) &= D^c_0(\vec{r}_{0,0}, t) + \left[D^c_0(\vec{r}_{1,0}, t) - D^c_0(\vec{r}_{0,0}, t)\right]\frac{u}{U} \\ &\quad + \left[D^c_0(\vec{r}_{0,1}, t) - D^c_0(\vec{r}_{0,0}, t)\right]\frac{v}{V} \\ &= D^c_0(\vec{r}_{0,0}, t) + \frac{\Delta D_u(t)}{U}\,u + \frac{\Delta D_v(t)}{V}\,v\end{aligned} \tag{31}$$

where

$$\Delta D_u(t) = D^c_0(\vec{r}_{1,0}, t) - D^c_0(\vec{r}_{0,0}, t) \tag{32}$$

$$\Delta D_v(t) = D^c_0(\vec{r}_{0,1}, t) - D^c_0(\vec{r}_{0,0}, t) \tag{33}$$

are the difference signals in the u- and v-directions, respectively.

4. Determination of Output Voltage from Rectangular Tile: By applying the expressions for the linearized delay, $\tau(u,v)$ in (18), and for the linearized diffraction response with the delay removed, $D_0(u,v,t)$ in (31), the output voltage, $v_{\text{tile}}(t)$, due to the tile can be expressed as:

$$v_{\text{tile}}(t) = K\int_0^U \int_0^V D_0(u,v,t) \otimes \delta(t - \tau(u,v))\,dv\,du \tag{34}$$

where the obliquity factor is omitted for clarity. The expression for $v_{\text{tile}}(t)$ in (34) can be expanded to:

$$\begin{aligned}v_{\text{tile}}(t) &= K D^c_0(\vec{r}_{0,0}, t) \otimes \int_0^U \int_0^V \delta(t - \tau(u,v))\,dv\,du \\ &\quad + K\frac{\Delta D_u(t)}{U} \otimes \int_0^U \int_0^V u\,\delta(t - \tau(u,v))\,dv\,du \\ &\quad + K\frac{\Delta D_v(t)}{V} \otimes \int_0^U \int_0^V v\,\delta(t - \tau(u,v))\,dv\,du.\end{aligned} \tag{35}$$

The term $\delta(t - \tau(u,v))$ can be expressed as:

$$\begin{aligned}\delta(t - \tau u, v)) &= \delta(t - \tau^c_{0,0} - \Gamma_u u - \Gamma_v v) \\ &= \delta(t - \tau^c_{0,0}) \otimes \delta(t - \Gamma_u u) \otimes \delta(t - \Gamma_v v).\end{aligned} \tag{36}$$

The derivation of the output voltage due to the tile from (35) is simplified by the fact that the double integrals are separable into single integrals along the u- and v-direction. The integrals are all of the types that were considered previously in the derivation of the solution for the line reflector in Appendix A. Analogous to the approach in (54)–(63), four filter functions can be defined:

$$X_u(t) = \int_0^U \delta(t - \Gamma_u\, u)\, du \tag{37}$$

$$Z_u(t) = \frac{1}{U}\int_0^U \delta(t - \Gamma_u\, u)\, u\, du \tag{38}$$

$$X_v(t) = \int_0^V \delta(t - \Gamma_v\, v)\, dv \tag{39}$$

$$Z_v(t) = \frac{1}{V}\int_0^V \delta(t - \Gamma_v\, v)\, v\, dv. \tag{40}$$

By using the procedure from (54)–(63), the filter functions can be found to be:

$$X_u(t) = \begin{cases} 1/\Gamma_u, & 0 \le t < U\Gamma_u,\ \Gamma_u > 0 \\ -1/\Gamma_u, & U\Gamma_u \le t < 0,\ \Gamma_u < 0 \\ \delta(t)U, & t = 0, \qquad \Gamma_u = 0 \\ 0, & \text{otherwise} \end{cases} \tag{41}$$

$$Z_u(t) = \begin{cases} t/(U\Gamma_u^2), & 0 \le t < U\Gamma_u,\ \Gamma_u > 0 \\ -t/(U\Gamma_u^2), & U\Gamma_u \le t < 0,\ \Gamma_u < 0 \\ \delta(t)U/2, & t = 0, \qquad \Gamma_u = 0 \\ 0, & \text{otherwise} \end{cases} \tag{42}$$

$$X_v(t) = \begin{cases} 1/\Gamma_v, & 0 \le t < V\Gamma_v,\ \Gamma_v > 0 \\ -1/\Gamma_v, & V\Gamma_v \le t < 0,\ \Gamma_v < 0 \\ \delta(t)V, & t = 0, \qquad \Gamma_v = 0 \\ 0, & \text{otherwise} \end{cases} \tag{43}$$

$$Z_v(t) = \begin{cases} t/(V\Gamma_v^2), & 0 \le t < V\Gamma_v,\ \Gamma_v > 0 \\ -t/(V\Gamma_v^2), & V\Gamma_v \le t < 0,\ \Gamma_v < 0 \\ \delta(t)V/2, & t = 0, \qquad \Gamma_v = 0 \\ 0, & \text{otherwise} \end{cases}. \tag{44}$$

Substituting (41)–(44) into (35) and (36) results in:

$$\begin{aligned} v_{\text{tile}}(t) = K\cos[\theta(\vec{r}_m)]\, \delta(t - \tau^c_{0,0}) \otimes \\ [D^c_0(\vec{r}_{0,0}, t) \otimes X_u(t) \otimes X_v(t) \\ + \Delta D_u(t) \otimes Z_u(t) \otimes X_v(t) \\ + \Delta D_v(t) \otimes X_u(t) \otimes Z_v(t)] \end{aligned} \tag{45}$$

where the obliquity factor is reintroduced, with the angle evaluated at the center of the tile, represented by vector $\vec{r}_m$. The calculation of the diffraction response integrated over the tile thus has been converted into calculation of the responses at the four corners and a number of time-domain convolutions. The output voltage from the entire reflector, $v_{\text{surf}}(t)$, is found by superposition, i.e., by summing the responses from all the individual tiles:

$$v_{\text{surf}}(t) = g_r(t) \otimes u_{tx}(t) \otimes \sum_{\text{all tiles}} v_{\text{tile}}(t) \tag{46}$$

in which the surface velocity of the transmitting transducer and the acousto-electric impulse response of the receiving transducer that were previously omitted for clarity have been re-introduced.

IV. Implementation of the DRIM

In this section an implementation of the DRIM will be presented for the case of a planar circular piston transducer of radius 12.7 mm as transmitter and receiver. During the implementation it was discovered that the changes in diffraction responses were dominated by unique time shifts of the individual segments rather than by amplitude scalings; consequently, the amplitude linearization did not improve the accuracy of the results for this transducer type. Therefore, a segmentation approach was implemented in which the responses are segmented and the individual segments are delay linearized individually.

A. Calculation of Diffraction Response

Efficient implementation of the DRIM by digital computation is not trivial. The difficulties in the implementation are in part due to the strong high frequency components in the velocity potential impulse responses and even more so in its time derivatives. Careful design considerations, therefore, must be made to reduce aliasing to an acceptable level in the frequency range of interest, which in this paper is chosen to be 0–15 MHz, appropriate for most medical and NDT-applications. The calculation of $D(\vec{r}, t)$ consists of the following operations:

- Calculation of the velocity potential impulse response for the transmit transducer, $h_t(\vec{r}, t)$, for the field point $\vec{r}$.
- Calculation of the velocity potential impulse response for the receive transducer, $h_r(\vec{r}, t)$, for the field point $\vec{r}$. When the receive transducer is identical to the transmit transducer then $h_r(\vec{r}, t) = h_t(\vec{r}, t)$ and this step is trivial.
- Convolution of $h_t(\vec{r}, t)$ and $h_r(\vec{r}, t)$.
- Double differentiation of the convolution result with respect to time.

A multi-rate digital signal processing algorithm is used to determine $h(\vec{r}, t)$, based on sampling of the analytical solutions that exist for several transducer geometries. The velocity potential impulse response for a planar circular piston transducer has an increasing high-frequency content as the field point moves closer to the transducer axis; here $h(\vec{r}, t)$ is a rectangular function. The algorithm uses a sampling frequency $f_s = 6.4$ GHz for field points close to or at the axis of symmetry, and a lower sampling frequency for field points further from the axis where the responses are longer and of a more low-frequency nature. This allows aliasing problems to be kept at a negligible level; with the selected parameters the amplitude of the aliased component is at least 52 dB below the true signal over the frequency range of interest. After sampling, the responses are low-pass filtered and decimated in a computationally

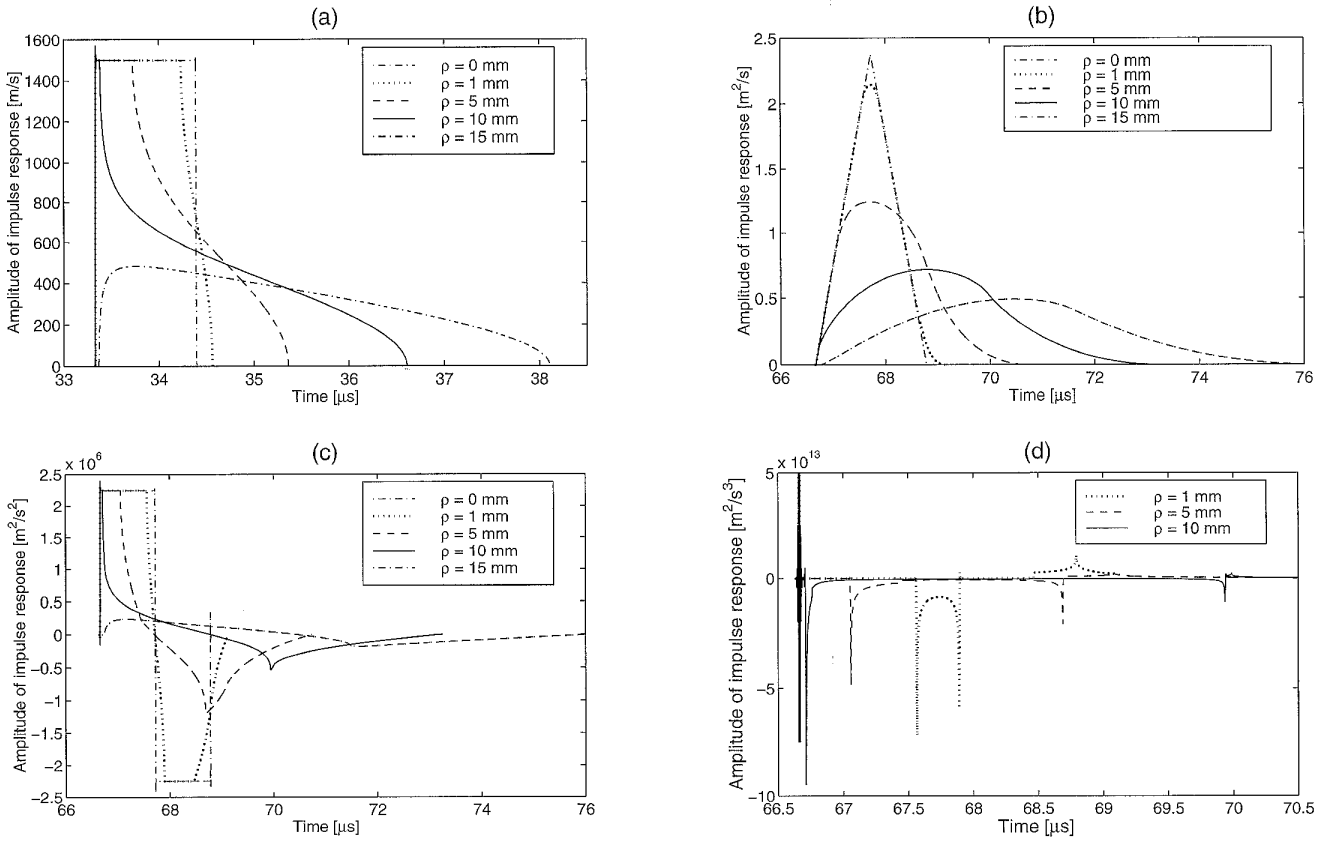

Fig. 6. The steps involved in the calculation of $D(\vec{r},t)$ for a 12.7 mm radius planar piston transducer. The axial distance is 50 mm and signals for radial distances of $\rho = 0$, 1, 5, 10, and 15 mm are shown, except in (d) where only signals for $\rho = 1$, 5, and 10 mm are shown. The speed of sound was 1500 m/s. $h(\vec{r},t)$ is seen in (a), $h(\vec{r},t) \otimes h(\vec{r},t)$ in (b), $\partial\left(h(\vec{r},t) \otimes h(\vec{r},t)\right)/\partial t$ in (c), and $D(\vec{r},t)$ in (d). For clarity the positively going impulses in (d) at $t \simeq 66.7$ μs have been truncated at $5 \cdot 10^{13}$ m^2/s^3, while they actually extend to $\simeq 5.5 \cdot 10^{14}$ m^2/s^3.

efficient combined filter-decimator, so that the digitized velocity potential impulse response from any field point is returned with $f_s = 400$ MHz. The algorithm is described in detail in [21]. An illustration of $h(\vec{r},t)$ for 5 different radial distances, calculated with this algorithm, is shown in Fig. 6(a). The next step in the calculation of $D(\vec{r},t)$ is the convolution of $h_t(\vec{r},t)$ and $h_r(\vec{r},t)$. An illustration of $h_t(\vec{r},t) \otimes h_r(\vec{r},t)$ for the five $h(\vec{r},t)$ curves in Fig. 6(a) is shown in Fig. 6(b). Notice that the convolved responses are of a more low-frequency nature than the original velocity potential impulse responses. In order to obtain $D(\vec{r},t)$, $h(\vec{r},t) \otimes h(\vec{r},t)$ must be differentiated twice. As the responses are sampled at a very high sampling frequency, the digital differentiation can be replaced by a simple difference operation and a delay compensation by one half sample period. The magnitude error introduced by this approximation is only 0.25% at $f_{\max} = 15$ MHz, which is an acceptable error level. If this differentiation approach is used for making a single differentiation on the responses in Fig. 6(b), the results are as illustrated in Fig. 6(c). Performing the second differentiation gives the desired diffraction responses $D(\vec{r},t)$, illustrated in Fig. 6(d). For clarity, only curves for radial distances of $\rho = 1$, 5 and 10 mm are shown, because curves for radial distances larger than the transducer radius are of such small amplitude that they cannot be properly observed.

B. Segmentation and Delay Filtering

In order to handle the unique time shifts of the individual segments of a diffraction response, a segmentation method was developed. As illustrated in Fig. 6(d) the diffraction responses generally consist of short "impulsive" segments, separated by regions of very low amplitude. A viable approach, therefore, is to divide the signals into segments, linearize the delay/time shift between corresponding segments from the four corners, calculate the contribution from each of the segments using the delay filtering approach, and then find the response from the tile as the sum of the responses from the individual segments. Consequently, each of the four responses are divided into a small number of segments, and the time shifts of the four corresponding segments, one from each of the four corners, are used to determine the delay filter response to be employed in the calculation of the integrated response over the tile surface for the actual segment, using the delay filtering technique described in Section III,B. This approach makes the delay filtering much more precise as the time

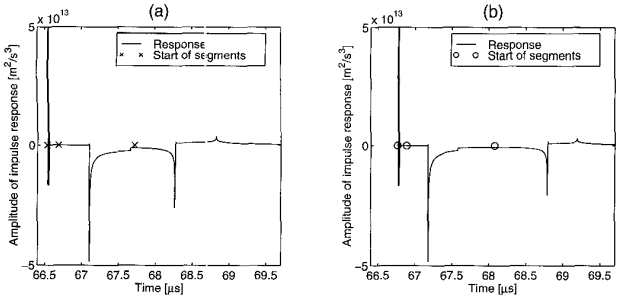

Fig. 7. Example of segmentation (3 segments) of diffraction responses from opposite corners of a 1×1 mm tile with its center at $(x, y, z) = (3, 3, 50)$ mm and tilted 10° in the y-direction. (a) The response for corner nearest to the acoustic axis, and (b) the response from the opposite corner. For clarity the positively going impulses (which have identical magnitudes) have been truncated as in Fig. 6.

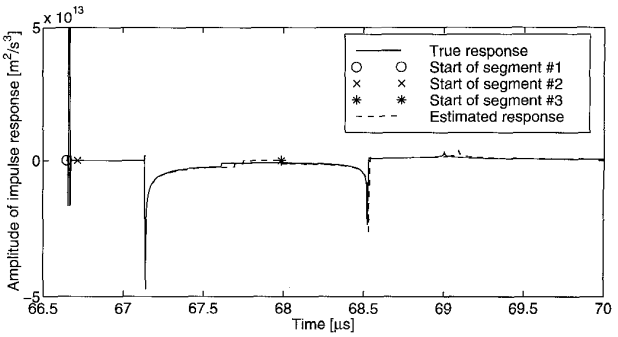

Fig. 8. Example of how well the estimated diffraction response compares to the true response at the center of a 1×1 mm tile with its center at $(x, y, z) = (3, 3, 50)$ mm and tilted 10° relative to the transducer surface. For clarity the positively going impulses have been truncated like in Fig. 6.

shifts of the individual segments can be rather different, depending on tile location, transducer type, etc.

1. Segmentation of Diffraction Responses: The approach to segmentation of a given diffraction response is as follows:

- The extrema of the response are found.
- The signal is segmented with one segment per extremum such that segment boundaries are at the time instance between the extremas where the amplitude is closest to zero.
- The signal amplitude at the boundary between any two segments is compared to the amplitudes of the surrounding two extrema; if the amplitude at the boundary is above a specified fraction (typically 0.2) of the smallest extremum, the two segments are merged into one segment.

This procedure allows only segments that are separated by a region of low amplitude to exist. This is important when the segments are delay filtered individually, then added to form the integrated response because a significant signal amplitude at the boundaries will result in discontinuities in the final signal when the segments are shifted in the time domain by the delay filters. An example of segmentation results for two opposite corners of a 1×1 mm tile is illustrated in Fig. 7. When the time shifts between corresponding segments from the responses of the four corners of the tile are to be determined, the temporal position of the maximum in each segment is used. This ensures that the region containing the highest amplitude is positioned correctly in the time domain, resulting in a good approximation to the true response. The creation of the delay filters in (41) and (43) is straightforward, and the integrated response is found by convolving the segment responses with the two filters as described in (45) (with the amplitude linearization terms omitted).

In order for the segmentation approach to work properly, the tile sizes must be chosen so the basic shape of the responses does not change much from corner to corner. Otherwise, the diffraction responses from the four corners may not be divided into an identical number of segments. The implemented algorithm has been found to work satisfactorily for square tiles with side lengths up to approximately 1.5 mm, with the present transducer type.

2. Validation of the Segmentation Approach: To assess the validity of the claim that the dominant changes in the diffraction response over the surface of a reasonably small tile can be described by time shifts of the corresponding segments of the diffraction responses from the four corners, an example will be presented in which the response at the center of a tile will be estimated by the delay linearization method and then compared to the true response at that field point. Note that the operation of estimating the response at a given point on the tile is only an intermediate step—the true goal is to calculate the response integrated over the entire tile surface.

A 1×1 mm tile, tilted 10° relative to the transducer surface, and positioned with its center at $(x, y, z) = (3, 3, 50)$ mm in front of the transducer is considered. If the diffraction responses from the four corners are calculated and segmented, the responses are found to divide into three segments. When these segments are time shifted as given by the delay linearization model described in Section III,B and added to form the total estimated response at the center of the tile, the result in Fig. 8 is obtained. The true response at the center of the tile is plotted in Fig. 8 for comparison. The time delay interpolation model approximates the true response very well, even though the responses at the four corners are significantly different, as is evident from Fig. 7, which considers the same tile and setup.

V. Results

A. Calculation of Response from a Single Tile

The DRIM will be used for calculating the output voltage due to a 1×1 mm tile positioned and oriented as the

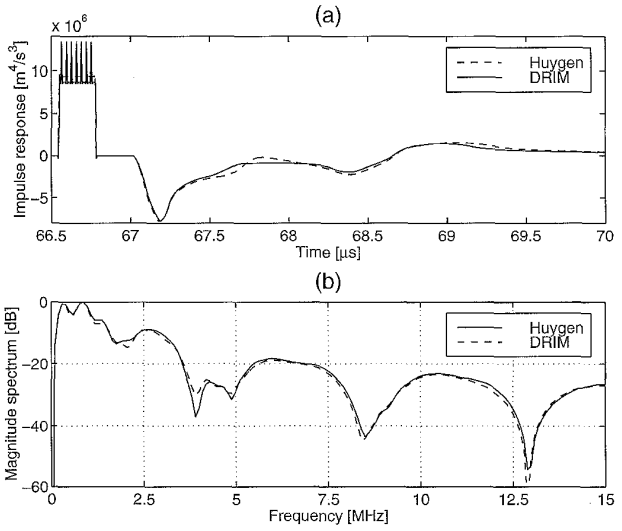

Fig. 9. The integrated diffraction response from a 1x1 mm tile with its center at $(x, y, z) = (3, 3, 50)$ mm. The response is shown as time signal (a) and spectrum (b). The tile is tilted 10° relative to the transducer surface. The resulting response is shown for two calculation methods, the DRIM and a simple method based on Huygen's principle.

TABLE I
COMPUTATION TIMES FOR OUTPUT VOLTAGE FROM 1 × 1 MM TILE.

Huygen's method	DRIM
398 s	1 s

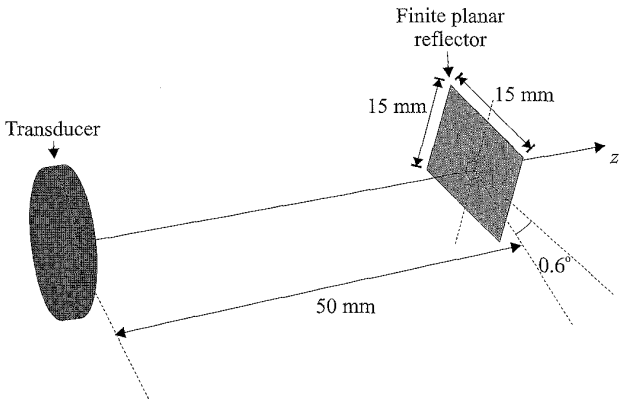

Fig. 10. The physical arrangement in which the transducer insonifies a 15x15 mm reflector centered on the acoustic axis and tilted 0.6°.

tile described in Fig. 8. The result of using the DRIM is shown in Fig. 9. The integrated response also is found by means of Huygen's principle, i.e., by calculating the responses at a large number of surface points and simply adding the responses. Specifically, the Huygen result in Fig. 9 shows the response found when using 50×50 evenly spaced surface points on the 1×1 mm tile, corresponding to a 20 μm spacing between points. The spacing of 20 μm was found by a "trial-and-error" method: Simulations using spacings of 10, 20, and 40 μm were made and while negligible difference between the results for 10 and 20 μm spacings was found, the results for 20 and 40 μm spacings differed somewhat. Note that the optimal point spacing for a given situation is very dependent on transducer type, tilt angle of the reflector surface, reflector location, etc.

The two output voltages, estimated with the two methods, agree very well, indicating that the DRIM gives accurate results, despite its inherent approximations. The first part of the time domain response calculated by means of the Huygen approach contains some very high frequency oscillations, originating from the discretization of the surface integral calculation. The consequence is that the strong impulses at the start of the responses are not effectively smoothed out unless an even larger number of surface points is used. However, the oscillations are of such high frequency that they do not give errors in the frequency range of interest, as is evident from the spectra in Fig. 9(b). The advantage of the DRIM is, however, not primarily a high accuracy, but rather a reduced calculation time, as evidenced by the computation times (using a HP 735 UNIX workstation) for the output voltage using the two methods, listed in Table I.

B. Comparison to Other Modeling Techniques

The DRIM will now be compared to two alternative modeling techniques, in order to compare accuracy and computational speed when calculating responses for extended reflectors. The two methods are the simple method using Huygen's principle and the angular spectrum decomposition (ASD) method described in [4].

This section will describe modeling of the output voltage from a transducer insonifying a planar 15×15 mm reflector, centered on the acoustic axis and tilted 0.6° as illustrated in Fig. 10. Modeling results from the three different methods are presented in Fig. 11 in the form of spectra of the time domain responses rather than as time signals, since the ASD method inherently produces frequency domain results. The result of the DRIM is based on 225 tiles of 1×1 mm, and the result using Huygen's technique is based on a total of 22,500 surface points (spacing of 100 μm). The three methods produce almost identical results even though the ASD method uses an entirely different modeling technique. The results presented in Fig. 11 also illustrate the extreme sensitivity of the output voltage from a planar circular piston transducer to the angle between the transducer axis and the surface normal of the planar reflector. These results also have been verified experimentally [4]. The computational efficiency of the DRIM is demonstrated by comparing the computation times of the diffraction responses for the three different methods as shown in Table II, using a HP 735 UNIX workstation. Furthermore, it must be noted that the modeling situation chosen here is not the one best suited for showing the efficiency and versatility of the DRIM. If a sur-

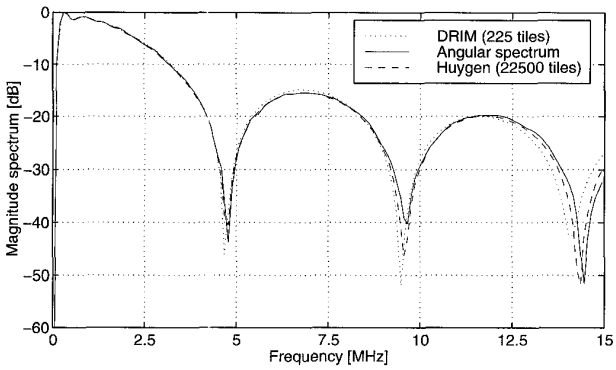

Fig. 11. Spectra of diffraction response from the transducer insonifying a 15 × 15 mm reflector centered on the acoustic axis and tilted 0.6°. The plot shows spectra obtained using the DRIM, an ASD technique, and Huygen's principle, respectively.

TABLE II
COMPUTATION TIMES FOR THE DRIM, AN ASD METHOD, AND HUYGEN'S METHOD FOR A 15 × 15 MM PLANAR REFLECTOR.

DRIM	Angular spectrum	Huygen's method
2.3 min	93 min	70 min

face with a larger tilt angle had been used, Huygen's technique would have required a much larger number of surface points in order to accurately reproduce the high frequency components of the output voltage, thus giving a larger difference in computational efficiency between the two methods. The angular spectrum technique, on the other hand, is far less general, requiring a separate modeling for *each* planar reflector (no restriction as to the size of each planar reflector applies here, however), thus resulting in extremely high computational burdens when handling irregular surfaces. The reason for choosing this specific modeling situation is the fact that both simulation and experimental results are available, thus ensuring a good validation of the DRIM.

C. Comparison of Numerical and Experimental Results

In this section the performance of the DRIM for surfaces of more complex geometry will be investigated. Specifically, a series of experimental pulse-echo measurements using a cylindrical reflector has been made and compared to numerical results.

A 20 mm diameter Plexiglas cylinder was placed with its axis perpendicular to the transducer axis, at an axial distance of 50 mm from the transducer surface and at varying radial distances from the transducer axis, as illustrated in Fig. 12. The transducer is a planar circular piston type (V307-SU, Panametrics Inc., Waltham, MA) with radius $a = 12.7$ mm and an estimated usable bandwidth of 4 MHz (center frequency 5 MHz). The transducer was connected to a pulser/receiver (Panametrics 5072 PR, Panametrics Inc.), and a digital sampling oscilloscope (LeCroy 9450,

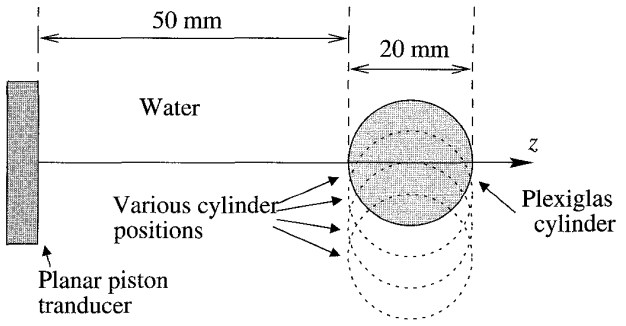

Fig. 12. Cross-sectional view of the experimental measurement situation, with cylinder at various radial distances from the transducer axis.

LeCroy Corp., Geneva, Switzerland) was used to digitize the output voltages. The signals were sampled using a sampling rate $f_s = 400$ MHz and averaged 50 times to reduce the influence of uncorrelated noise. The output voltage due to the front of the cylinder surface was extracted from the signal by time-gating to avoid reflections from the rear part of the cylinder and signals due to other reflection phenomena. The transducer was mounted in a 3D translation system (type 403020, Dyrbæk Technologies, Åbenrå, Denmark), allowing precise control of the measurement positions.

The calculations corresponding to the measurements were made by modeling the output voltages from the front part of cylinders of length 50 mm, placed similarly to the locations in the experiments. The front part of the cylinder (i.e., the part facing the insonifying transducer) was tessellated into square tiles with side lengths of 0.5 mm and the output voltage calculated as described in (46).

Time-domain results were created by finding the predicted output voltage, $v_{\text{pred}}(t)$, from the cylinder, based on the integrated diffraction response for the cylinder, $v_{\text{cyl}}(t)$; the following experimentally or numerically determined voltages: the integrated diffraction response from the large planar reflector, $v_{\text{ref}}(t)$; and the experimentally determined output voltage due to the large planar reflector, $v_{\text{ref,exp}}(t)$. This predicted output voltage was then compared to the experimentally determined output voltage from the cylinder, $v_{\text{cyl,exp}}(t)$. The shape of $v_{\text{ref,exp}}(t)$ is very close to the shape of the transducers combined electro-acoustic and acousto-electric impulse responses convolved with the excitation voltage (i.e., $g_r(t) \otimes u_{tx}(t)$). This is demonstrated by the fact that the integrated diffraction response, $v_{\text{ref}}(t)$, from a large planar reflector (e.g., 50 × 50 mm) positioned perpendicularly to the transducer axis is very close to a Dirac's delta function. Therefore, the predicted output voltage due to the cylinder can be found as:

$$v_{\text{pred}}(t) = C\, v_{\text{cyl}}(t) \otimes v_{\text{ref,exp}}(t) \tag{47}$$

where C is a constant scale factor, introduced to compensate for the different energies in the integrated diffraction response and experimentally determined reference output

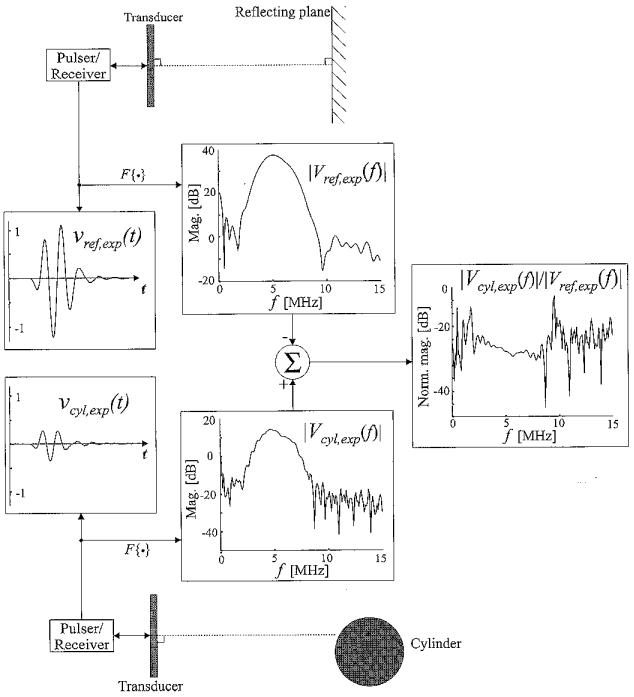

Fig. 13. Procedure for calculating the normalized magnitude spectrum, $|V_{\mathrm{cyl,exp}}(f)|/|V_{\mathrm{ref,exp}}(f)|$. $F\{\cdot\}$ denotes taking the Fourier transform, $v_{\mathrm{ref,exp}}(t)$ is the output voltage from a large planar reflector, perpendicular to the axis of the transducer, and $V_{\mathrm{ref,exp}}(f)$ is $F\{v_{\mathrm{ref,exp}}(t)\}$. $v_{\mathrm{cyl,exp}}(t)$ is the output voltage from the cylindrical surface, positioned at a given lateral distance off the axis of the transducer, and $V_{\mathrm{cyl,exp}}(f)$ is $F\{v_{\mathrm{cyl,exp}}(t)\}$.

voltage from the large planar reflector:

$$C = \sqrt{\frac{\int_{-\infty}^{\infty} v_{\mathrm{ref,exp}}^2(t)\,dt}{\int_{-\infty}^{\infty} (v_{\mathrm{ref}}(t) \otimes v_{\mathrm{ref,exp}}(t))^2\,dt}}. \tag{48}$$

Normalized results in the frequency domain were made by normalizing the spectra of the output voltages from the cylinders, $V_{\mathrm{cyl,exp}}(f)$, with the spectrum of the output voltage from a large planar reflector, $V_{\mathrm{ref,exp}}(f)$, positioned at the same axial distance and oriented perpendicular to the transducer axis. The normalization procedure is illustrated in Fig. 13. This procedure also was used for creating the normalized spectra for the simulation results.

Examples of experimental and simulation results are shown in Figs. 14 and 15, with time-domain results in (a) and normalized spectra for the experimental and simulated cases in (b). In Fig. 14 where the 20 mm diameter cylinder was placed symmetrically on the transducer axis the signal *level* is predicted very accurately, whereas there is a little bit more "ringing" in the predicted signal than in the experimental signal. From the normalized spectra, it is observed that the cylindrical geometry results in an attenuation of about 20 dB, relative to the planar reflector. Also, it can be noted that the frequency response has a slight low-pass character, probably due to phase cancellation being more pronounced at higher frequencies. In

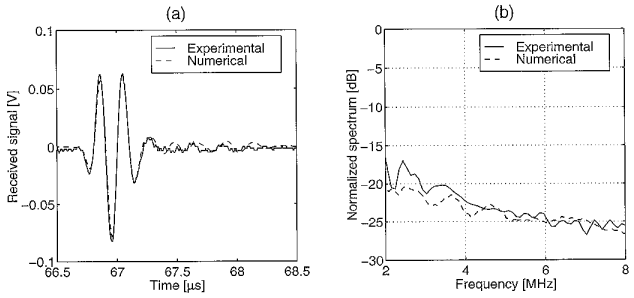

Fig. 14. Numerical and experimental time signals (a) and normalized spectra (b) from 20 mm diameter cylinder, placed symmetrically on the transducer axis, and at an axial distance of 50 mm from the transducer.

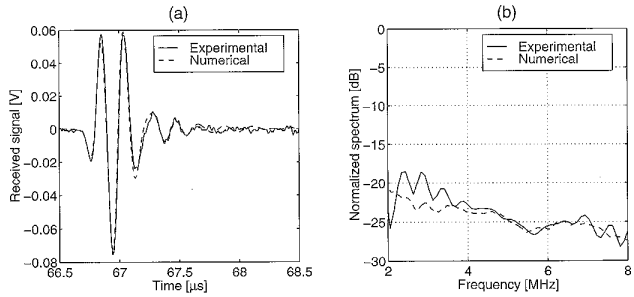

Fig. 15. Numerical and experimental time signals (a) and normalized spectra (b) from 20 mm diameter cylinder, placed 5 mm off the transducer axis, and at an axial distance of 50 mm from the transducer.

Fig. 15 in which the 20 mm diameter cylinder was placed 5 mm off the transducer axis, the signal *level* is again predicted very accurately. In this case a small characteristic "dip" in the spectrum around 5.5 MHz seems to be predicted by the numerical modeling. The effect of the correct prediction of the "dip" in the spectrum also is seen to result in a precise prediction of the time signal, which is seen to have a somewhat prolonged "tail".

VI. Discussion and Conclusions

This paper has presented a new computational approach, the diffraction response interpolation method (DRIM), for determining the output voltage in a pulse-echo system insonifying a reflector surface of arbitrary geometry. The method operates by tessellating the surface into rectangular tiles and finding the response as the sum of the responses from the individual tiles. The response from an individual tile is found using a linearization approach that leads to a computationally efficient implementation in which the response integrated over the tile is found by time domain convolution of the diffraction responses from the corners with analytically determined filters. The DRIM is based on linearity; therefore, effects such as shadowing, higher-order diffraction phenomena, and inhomogeneous media cannot be incorporated into the modeling.

The use of rectangular elements requires the introduction of least squares approximations in the linearization, which leads to a situation in which the field quantities are not steady at the boundaries between adjacent tiles. The error introduced by this phenomenon is difficult to predict quantitatively, but the modeling results indicate that significant degradation does not occur. The least squares approximation can be avoided if an analytical solution for triangular tiles can be developed, and the authors are currently pursuing this goal.

The DRIM is not applicable for modeling of situations including inhomogeneous propagation media, nonideal transducer behavior, etc., and neither are other impulse response based methods. Furthermore, there are some limitations on the acceptable reflector geometries due to the application of linearity, as described in Section II. One modeling technique capable of handling these more complicated situations is the finite-element based method. However, even the most advanced finite-element approaches published to date [7], [8] do not include effects of an inhomogeneous propagation medium. The finite-element methods are also believed to be slower than the DRIM in providing the solution for a specific situation, although no data on computation times are available for comparison. Thus, the choice of preferred modeling technique must be made depending on the requirements for each particular modeling.

The comparison to the Huygen method for a single 1×1 mm tile showed that the DRIM gives similar results using a 400 times smaller computation time. DRIM results for a 15×15 mm reflector at a small tilt angle were compared to results obtained using alternative techniques and an excellent agreement is seen. In this case the computation times were reduced by a factor of 30 to 40 compared to the alternative techniques. Thus, the goal of lowering the computation time while maintaining a high precision is achieved. Finally, DRIM results were compared to experimental results. A reasonably good agreement was found between modeling results and experimental data, especially near the center frequency of the transducer, where the signal-to-noise ratio is best. The signal levels are predicted quite accurately, whereas the finer structures of the spectra are not always reproduced very well. However, it is difficult to control the measurement situation well enough to ensure that the measurement and the simulation setup are in fact identical. For example, the alignment of transducer and reflector is known to be critical for planar transducers [4], and the vibrational pattern of the transducer may differ from the assumed constant piston movement behavior.

In conclusion, the DRIM has been found to be a precise and computationally efficient modeling tool for the output voltage in pulse-echo systems, when reflector surfaces of arbitrary geometry are investigated.

APPENDICES

A. Derivation of Linearization Filters

Equation (14) contains integrals of the form:

$$A_i(t) = \int_0^{S_i} \delta(t - \tau_i(l))\, dl \tag{49}$$

and

$$B_i(t) = \frac{1}{S_i} \int_0^{S_i} \delta(t - \tau_i(l)) l\, dl \tag{50}$$

The nature of the integrals in (49) and (50) will now be investigated. The linearized time delay function, $\tau_i(l)$, given in (12) can be expressed as:

$$\tau_i(l) = \tau_i + \alpha_i l, \quad l \in [0; S_i] \tag{51}$$

where α_i is the *delay slope* along the ith segment of the line reflector:

$$\alpha_i = \frac{\tau_{i+1} - \tau_i}{S_i}. \tag{52}$$

By introducing (51), the Dirac's delta function in (49) and (50) can be written as:

$$\delta(t - \tau_i(l)) = \delta(t - \tau_i - \alpha_i l) = \delta(t - \tau_i) \otimes \delta(t - \alpha_i l). \tag{53}$$

Applying (53) to (49) and (50) gives:

$$\begin{aligned} A_i(t) &= \int_0^{S_i} \delta(t - \tau_i) \otimes \delta(t - \alpha_i l)\, dl \\ &= \delta(t - \tau_i) \otimes \int_0^{S_i} \delta(t - \alpha_i l)\, dl \end{aligned} \tag{54}$$

$$\begin{aligned} B_i(t) &= \frac{1}{S_i} \int_0^{S_i} \delta(t - \tau_i) \otimes \delta(t - \alpha_i l) l\, dl \\ &= \delta(t - \tau_i) \otimes \frac{1}{S_i} \int_0^{S_i} \delta(t - \alpha_i l) l\, dl. \end{aligned} \tag{55}$$

By applying a change in variables, $\gamma = \alpha_i l$, (54) and (55) can be rewritten as:

$$A_i(t) = \delta(t - \tau_i) \otimes \frac{1}{\alpha_i} \int_0^{\alpha_i S_i} \delta(t - \gamma)\, d\gamma \tag{56}$$

$$B_i(t) = \delta(t - \tau_i) \otimes \frac{1}{S_i \alpha_i^2} \int_0^{\alpha_i S_i} \delta(t - \gamma) \gamma\, d\gamma. \tag{57}$$

The integrals in (56) and (57) are recognized to be of the form:

$$g(t) = \int_{\gamma_1}^{\gamma_2} \delta(t - \gamma) f(\gamma)\, d\gamma \tag{58}$$

Observe that $g(t)$ will only be nonzero for $t \in [\gamma_1; \gamma_2]$. Hence, $g(t)$ evaluates to be:

$$g(t) = \begin{cases} f(t), & \gamma_1 \le t \le \gamma_2 \text{ for } \gamma_1 < \gamma_2 \\ -f(t), & \gamma_2 \le t \le \gamma_1 \text{ for } \gamma_1 > \gamma_2 \\ 0, & \text{otherwise} \end{cases} \tag{59}$$

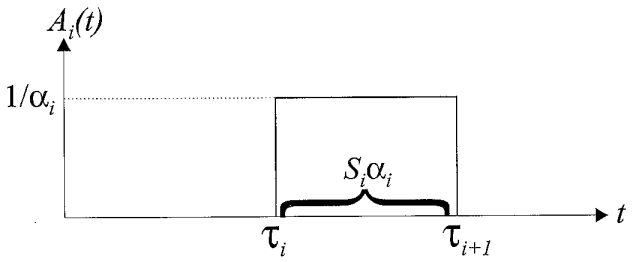

Fig. 16. Schematic illustration of $A_i(t)$ for a positive delay slope α_i.

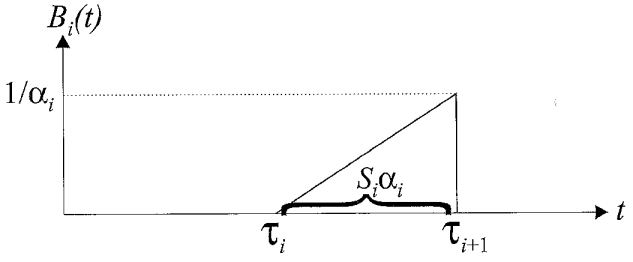

Fig. 17. Schematic illustration of $B_i(t)$ for a positive delay slope α_i.

Observe that the total area under $A_i(t)$ will always equal S_i:

$$\begin{aligned}\int_{-\infty}^{\infty} A_i(t)dt &= \int_{-\infty}^{\infty}\int_{0}^{S_i} \delta(t-\tau_i-\alpha_i l)\,dl\,dt \\ &= \int_{0}^{S_i}\int_{-\infty}^{\infty} \delta(t-\tau_i-\alpha_i l)\,dt\,dl \\ &= \int_{0}^{S_i} dl = S_i.\end{aligned} \tag{60}$$

Using the result of (59) and (60) for evaluating $A_i(t)$ gives:

$$A_i(t) = \begin{cases} 1/\alpha_i, & \tau_i \le t \le \tau_{i+1},\ \alpha_i > 0 \\ -1/\alpha_i, & \tau_{i+1} \le t \le \tau_i,\ \alpha_i < 0 \\ S_i\delta(t-\tau_i), & t=\tau_i, \quad \alpha_i = 0 \\ 0, & \text{otherwise} \end{cases}. \tag{61}$$

A schematic illustration of $A_i(t)$ for a positive α_i is given in Fig. 16.

A similar evaluation of the total area under $B_i(t)$ gives:

$$\begin{aligned}\int_{-\infty}^{\infty} B_i(t)\,dt &= \int_{-\infty}^{\infty}\frac{1}{S_i}\int_{0}^{S_i} \delta(t-\tau_i-\alpha_i l) l\,dl\,dt \\ &= \frac{1}{S_i}\int_{0}^{S_i}\int_{-\infty}^{\infty} \delta(t-\tau_i-\alpha_i l)\,dt l\,dl \\ &= \frac{1}{S_i}\int_{0}^{S_i} l\,dl = \frac{S_i}{2}.\end{aligned} \tag{62}$$

Using the results of (59) and (62) for evaluating $B_i(t)$ gives:

$$B_i(t) = \begin{cases} (t-\tau_i)/(S_i\alpha_i^2), & \tau_i \le t \le \tau_{i+1},\ \alpha_i > 0 \\ -(t-\tau_i)/(S_i\alpha_i^2), & \tau_{i+1} \le t \le \tau_i,\ \alpha_i < 0 \\ S_i/2\delta(t-\tau_i) & t=\tau_i, \quad \alpha_i = 0 \\ 0, & \text{otherwise} \end{cases} \tag{63}$$

A schematic illustration of $B_i(t)$ for a positive α_i is given in Fig. 17.

B. Least Squares Approximation of Delay Plane

An illustration of an "adjusted" least squares delay linearization plane is shown in Fig. 18. By application of (17)–(20) the following system of equations can be found:

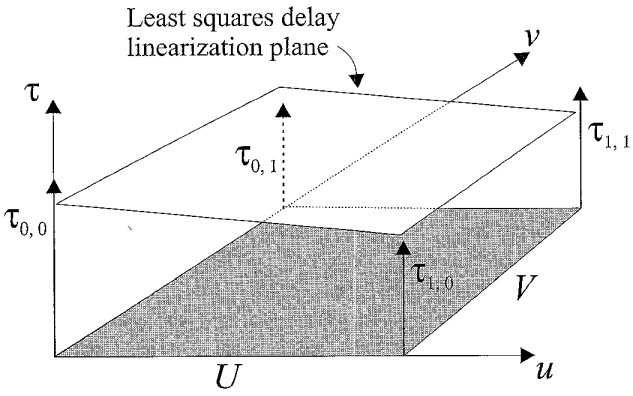

Fig. 18. Least squares delay linearization plane for the four values of τ from the corners of a rectangular tile.

$$\begin{aligned}\tau_{0,0} &= \tau^c_{0,0} + \epsilon_{0,0} \\ \tau_{1,0} &= \tau^c_{0,0} + \Gamma_u U + \epsilon_{1,0} \\ \tau_{0,1} &= \tau^c_{0,0} + \Gamma_v V + \epsilon_{0,1} \\ \tau_{1,1} &= \tau^c_{0,0} + \Gamma_u U + \Gamma_v V + \epsilon_{1,1}\end{aligned} \tag{64}$$

or expressed in matrix notation:

$$\begin{bmatrix}\tau_{0,0}\\ \tau_{1,0}\\ \tau_{0,1}\\ \tau_{1,1}\end{bmatrix} = \begin{bmatrix}1 & 0 & 0\\ 1 & U & 0\\ 1 & 0 & V\\ 1 & U & V\end{bmatrix}\begin{bmatrix}\tau^c_{0,0}\\ \Gamma_u\\ \Gamma_v\end{bmatrix} + \begin{bmatrix}\epsilon_{0,0}\\ \epsilon_{1,0}\\ \epsilon_{0,1}\\ \epsilon_{1,1}\end{bmatrix} \tag{65}$$

or in symbolic compact matrix form:

$$\mathbf{D} = \mathbf{S}\boldsymbol{\beta} + \boldsymbol{\epsilon} \tag{66}$$

The least squares solution to (66) can be found by applying the linear algebra method of orthogonal projections [22] to be:

$$\boldsymbol{\beta} = (\mathbf{S}^{\mathbf{T}}\mathbf{S})^{-1}\mathbf{S}^{\mathbf{T}}\mathbf{D} \tag{67}$$

where $\mathbf{A}^{\mathbf{T}}$ denotes the transpose of matrix $\mathbf{A}$. The result of the least squares solution is given in (21)–(23).

REFERENCES

[1] T. L. Rhyne, "Radiation coupling of a disk to a plane and back or a disk to a disk: An exact solution," *J. Acoust. Soc. Amer.*, vol. 61, no. 2, pp. 318–324, 1977.

[2] X. Chen, K. Q. Schwarz, and K. J. Parker, "Acoustic coupling from a focused transducer to a flat plate and back to the transducer," *J. Acoust. Soc. Amer.*, vol. 95, no. 6, pp. 3049–3054, 1994.

[3] D. P. Orofino and P. C. Pedersen, "Efficient angular spectrum decomposition of acoustic sources. Part II: Results," *IEEE Trans. Ultrason., Ferroelect., Freq. Contr.*, vol. 40, no. 3, pp. 250–257, 1993.

[4] P. C. Pedersen and D. P. Orofino, "Modeling of received ultrasound signals from finite planar targets," *IEEE Trans. Ultrason., Ferroelect., Freq. Contr.*, vol. 43, no. 2, pp. 303–311, 1996.

[5] B. J. Dean and P. C. Pedersen, "Angular spectrum based formulation of rough surface scattering with applications to surface characterization," *Proc. IEEE Ultrason. Symp.*, vol. 1, San Antonio, TX, 1996, pp. 693–696.

[6] R. Lerch, "Simulation of piezo-electric devices by two- and three-dimensional finite elements," *IEEE Trans. Ultrason., Ferroelect., Freq. Contr.*, vol. 37, pp. 233–247, 1990.

[7] R. Lerch, H. Landes, and F. Lindinger, "Piezoelectric CAD-system," in *Sensor 95*, (Wunstorf-Steinhude, Germany), pp. 297–302, ACS Organisations GmbH, 1995.

[8] R. Lerch, H. Landes, and H. T. Kaarmann, "Finite element modeling of the pulse-echo behavior of ultrasound transducers," *Proc. IEEE Ultrason. Symp.*, Cannes, France, Nov. 1994, pp. 1021–1025.

[9] G. R. Harris, "Review of transient field theory for a baffled planar piston," *J. Acoust. Soc. Amer.*, vol. 70, no. 1, pp. 10–20, 1981.

[10] J. A. Jensen, D. Gandhi, and W. D. O'Brien, "Ultrasound fields in an attenuating medium," *Proc. IEEE Ultrason. Symp.*, vol. 2, Cannes, France, 1993, pp. 943–946.

[11] M. A. Fink and J.-F. Cardoso, "Diffraction effects in pulse-echo measurement," *IEEE Trans. Sonics Ultrason.*, vol. 31, no. 4, pp. 313–329, 1984.

[12] J. A. Jensen and P. Munk, "Computer phantoms for simulating ultrasound B-mode and CFM images," in *Proc. 23rd Acoust. Imaging Symp.*, Boston, MA, Apr. 1997.

[13] D. R. Foster, M. Arditi, F. S. Foster, M. S. Patterson, and J. W. Hunt, "Computer simulations of speckle in B-scan images," *Ultrason. Imaging*, vol. 5, pp. 308–330, 1983.

[14] A. T. Kerr and J. W. Hunt, "A method for computer simulations of Doppler color flow images. 1. Theory and numerical method," *Ultrason. Med. Biol.*, vol. 18, no. 10, pp. 861–872, 1992.

[15] M. Ueda and H. Ichikawa, "Analysis of an echo signal reflected from a weakly scattering volume by a discrete model of the medium," *J. Acoust. Soc. Amer.*, vol. 70, no. 6, pp. 1768–1775, 1981.

[16] S. McLaren and J. P. Weight, "Transmit-receive mode responses from finite-sized targets in fluid media," *J. Acoust. Soc. Amer.*, vol. 82, no. 6, pp. 2102–2112, 1987.

[17] A. Lhémery, "Impulse response method to predict echo-responses from targets of complex geometry. Part I: Theory," *J. Acoust. Soc. Amer.*, vol. 90, no. 5, pp. 2799–2807, 1991.

[18] A. Lhémery and R. Raillon, "Impulse response method to predict echo-responses from targets of complex geometry. Part II: Computer implementation and experimental verification," *J. Acoust. Soc. Amer.*, vol. 95, no. 4, pp. 1790–1800, 1994.

[19] S. J. Oh, Y. C. Shin, and E. S. Furgason, "Surface roughness evaluation via ultrasonic scanning," *IEEE Trans. Ultrason., Ferroelect., Freq. Contr.*, vol. 41, no. 6, pp. 863–871, 1994.

[20] J. P. Weight and A. J. Hayman, "Observation of the propagation of very short ultrasonic pulses and their reflection by small targets," *J. Acoust. Soc. Amer.*, vol. 63, no. 2, pp. 396–404, 1978.

[21] D. P. Orofino and P. C. Pedersen, "Multirate digital signal processing algorithm to calculate complex acoustic pressure fields," *J. Acoust. Soc. Amer.*, vol. 92, no. 1, pp. 563–582, 1992.

[22] G. Strang, *Linear Algebra and its Applications*, 2nd ed., New York: Academic Press, 1980.

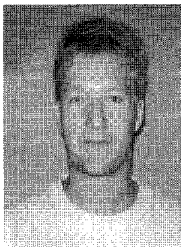

Søren K. Jespersen was born in Holbæk, Denmark, on March 4, 1968. He received the M.Sc. EE from the Technical University of Denmark (DTU) in 1994, and has until November 30, 1997, been an industrial research Ph.D. student at B-K Medical and at the Department of Information Technology, DTU. He currently is employed as development engineer at B-K Medical, Gentofte, Denmark.

His current research interests include improvement of diagnosis of atherosclerotic disease using ultrasound and modeling of pulse-echo systems.

Peder C. Pedersen (S'74-M'76-SM'87) was born in Kalundborg, Denmark. He received the B.S. degree in electrical engineering from Aalborg Engineering College, Aalborg, Denmark, in 1971, and the M.E. and Ph.D. degrees in bioengineering from the University of Utah, Salt Lake City, in 1974 and 1976, respectively. In October 1987 he joined the faculty at Worcester Polytechnic Institute in Worcester, MA. He is a professor in the Electrical and Computer Engineering Department. Previously, he was an Associate Professor in the Department of Electrical and Computer Engineering at Drexel University, Philadelphia, and a core faculty member of Drexel's Biomedical Engineering and Science Institute.

His research areas include modeling of acoustic systems; characterization of rough surfaces based on scattered signals; Doppler flow systems utilizing FM excitation; and ultrasound-based measurement of mechanical properties of blood vessels. Specific applications include characterization of atherosclerotic plaque and ultrasound-based assessment of osteoporosis.

Dr. Pedersen is a member of Eta Kappa Nu, Sigma Xi, the Acoustical Society of America, and a senior member of the IEEE. He is an Advisory Board member of CRC Critical Reviews in Biomedical Engineering and a Registered Professional Engineer in the Commonwealth of Pennsylvania.

Jens E. Wilhjelm (S'86–M'86–S'88–M'91) was born in Copenhagen, Denmark. He received the M.Sc. degree in electrical engineering from the Technical University of Denmark in 1986 and the Ph.D. degree in biomedical engineering in 1991 from Worcester Polytechnic Institute, Worcester, MA. From 1986 to 1988 he worked with blood flow measurements in the ultrasonic laboratory at Brüel & Kjær A/S, Nærum, Denmark. In 1991, he came to the Electronics Institute, Technical University of Denmark where he held various fellowship positions until he became an associate professor in 1997 at the Department of Information Technology.

His current research interests in medical diagnostic ultrasound includes technical and medical aspects within classification of atherosclerotic plaque, signal processing, and Doppler based blood flow measurements.

Dr. Wilhjelm is a member of the IEEE.